Dynamic Polarizability of the ^{85}Rb $5D_{3/2}$-State in 1064 nm Light

Alisher Duspayev [ID]*, **Ryan Cardman** [ID] **and Georg Raithel** [ID]

Department of Physics, University of Michigan, Ann Arbor, MI 48109, USA
* Correspondence: alisherd@umich.edu

Abstract: We report a measurement of the dynamic (ac) scalar polarizability of the $5D_{3/2}$ state in ^{85}Rb atoms at a laser wavelength of 1064 nm. Contrary to a recent measurement in Phys. Rev. A 104, 063304 (2021), the experiments are performed in a low-intensity regime in which the ac shift is less than the $5D_{3/2}$ state's hyperfine structure, as utilized in numerous experiments with cold, trapped atoms. The extracted ac polarizability is $\alpha_{5D_{3/2}} = -499 \pm 59$ a.u., within the uncertainty of the aforementioned previous result. The calibration of the 1064 nm light intensity, performed by analyzing light shifts of the D1 line, is the main source of uncertainty. Our results are useful for applications of the Rb $5D_{3/2}$ state in metrology, quantum sensing, and fundamental-physics research on Rydberg atoms and molecules.

Keywords: precision measurements; dynamic polarizability; optical lattices; photo-ionization

1. Introduction

Precision measurements of atomic structure and properties are of major importance for a wide range of applications including optical atomic clocks [1–3], quantum computing and simulations [4,5], and field sensing [6–9]. Atom–field interactions are an essential tool in a variety of these topics, as quite often it is required to trap neutral atoms, perform optical or microwave excitations and enhance or mitigate certain effects. Shifts of atomic energy levels due to the ac Stark effect [10–12], ΔW, can be listed among such effects and are described (in terms of the local field intensity I) by (in SI units):

$$\Delta W = -\frac{\alpha_\xi(\lambda)I}{2c\epsilon_0}, \tag{1}$$

where $\alpha_\xi(\lambda)$ is the ac polarizability of an atomic state $|\xi\rangle$ at the wavelength of the applied field, λ, c is the speed of light, and ϵ_0 is the vacuum permittivity. Determination of $\alpha_\xi(\lambda)$ is crucial for applications of certain atomic or molecular states that involve atom–field interactions [13–16] including laser cooling and trapping [17], quantum control [18,19], and optical clocks [1–3].

In this paper, we report a measurement of α for the $5D_{3/2}$ state of ^{85}Rb atom at $\lambda = 1064$ nm. This wavelength is widely used for optical dipole traps and lattices for both neutral atoms [20] and ions [21] because it is a commonly available wavelength emitted at high optical powers from diode and Nd:YAG fiber lasers. A recent measurement at this wavelength yielded a result of $\alpha_{5D_{3/2}} = -524 \pm 17$ (in atomic units) [22]. The experiment in [22] was performed at an intensity on the order of $100\ \mathrm{GW/m^2}$, which is high enough to decouple the hyperfine (HF) structure and to cause large broadening due to photoionization (PI), as 1064 nm is above the PI threshold of the $5D_{3/2}$ state (1251.52 nm). However, it is not always desirable [4] or even practical to conduct experiments under such high-intensity conditions. In the present work, we therefore perform two-photon spectroscopy of the ac Stark effect of the $5D_{3/2}$ state and measure $\alpha_{5D_{3/2}}$ at low intensity of the 1064-nm light, where HF interactions are on the same order as the light shifts.

The $5D$ states of Rb are of general interest for several reasons. Two-photon transitions between the ground, $5S_{1/2}$, and $5D_J$ states are relatively strong, narrow and can be driven by lasers in readily accessible visible or NIR ranges. These features make the aforementioned transitions attractive in metrology and as frequency references [3,23–28]. Moreover, Rb atoms in $5D_J$ states can be excited into Rydberg nP and nF states for studies on three-photon EIT [29,30], Rydberg molecules [31], and spectroscopy of high-angular-momentum Rydberg states [32,33]. For the Rb $5D_{3/2}$ state, the static polarizability [34], the HF structure [23,35], the radiative lifetime [36], and, recently, the dynamic polarizability at 1064 nm [22] have been measured. In addition, the large PI cross-section of the $5D_{3/2}$ state [22,37,38] could be used for generation of ultracold plasmas [39,40] and experiments on atom–ion interactions [41–44].

Our paper is organized as follows: theoretical considerations of atom–light interactions and details of the experimental setup and the data analysis are provided in Section 2. Results are presented and discussed in Section 3. The paper is concluded in Section 4.

2. Methods

2.1. Theoretical Background

Assuming a linearly polarized field, α_ξ in Equation (1) can be expressed as

$$\alpha_\xi(\lambda) = \alpha_\xi^{(0)}(\lambda) + \eta_\xi \alpha_\xi^{(2)}(\lambda), \tag{2}$$

where $\alpha_\xi^{(0)}$ and $\alpha_\xi^{(2)}$ are referred to as scalar and tensor dynamic polarizabilities, respectively, with the latter vanishing for states with $J < 1$. The elements of the second-rank tensor η_ξ depend on the eigenstates of the Hamiltonian that describe the atom–field interaction. Circular polarization components would require an additional term proportional to the vector polarizability, $\alpha_\xi^{(1)}$, which is not included in Equation (2) because in our experiment the light interacting with the atoms has been experimentally confirmed to be linearly polarized, with an upper limit of the polarization imperfection of 0.4%. Therefore, the vector part is insignificant in our present experiment. Furthermore, as the 1064-nm laser light used in our work is far-off-resonant from all transitions from the $5S_{1/2}$ and $5P_{1/2}$-levels, hyperfine-induced tensor contributions to the $5S_{1/2}$- and $5P_{1/2}$-polarizabilities are negligible here. Using calculations similar to those presented in [45], we are estimating magnitudes of the $5S_{1/2}$ and $5P_{1/2}$ tensor relative to the scalar polarizabilities on the order of 10^{-5} and 10^{-4}, respectively. Hence, in our modeling in Section 3, we ignore $5S_{1/2}$ and $5P_{1/2}$ tensor polarizabilities.

Depending on the strength of the applied field, the system can be dominated by the HF structure of the atom (weak-field case), the atom–light coupling (strong-field case) or reside in the intermediate regime. Comparing the system with an atom in an external magnetic field, the first two cases are analogous to the Zeeman and Paschen–Back regimes of the HF structure, respectively. The weak- and strong-field sets of the eigenstates are generally different. In the weak-field regime, the eigenstates of the Hamiltonian are given by the $\{|F, m_F\rangle\}$-basis, with HF quantum numbers F and m_F. An ac Stark interaction significantly larger than the HF interaction mixes the $\{|F, m_F\rangle\}$ states, and the set of time-independent states approaches the $\{|m_J, m_I\rangle\}$-basis, with magnetic quantum numbers m_J and m_I denoting electronic and nuclear spin along the lattice laser's electric-field direction. In the intermediate lattice-intensity regime, the time-independent states transition from the low-field into the high-field basis [46,47]. Analytical expressions for the elements of η_ξ can be derived in the weak- and strong-field cases (see, e.g., [48]). Under the presence of level broadening due to PI in the lattice–laser field, and if the tensor contribution of the polarizability is small, the transition of the time-independent states from the $\{|F, m_F\rangle\}$ into the $\{|m_J, m_I\rangle\}$-basis may be blurred, as is the case for Rb $5D_{3/2}$ state in 1064-nm light. A previous measurement of $\alpha_{5D_{3/2}}$ [22] has been performed in the strong-field regime. In the present work, we conduct an experiment in the low-field regime. In the case that there are no unaccounted-for systematic errors in either of the measurements, the polarizabilities

derived from the data should agree between low- and high-field measurements. The experimental challenges of the present low-field measurement and the methods employed to address them are described in Section 2.4.

2.2. Experimental Setup

Our measurements are performed using ^{85}Rb atoms cooled within an intracavity optical lattice (OL). Detailed design and characterization of the utilized setup are provided in [49]. The essential aspects of the apparatus are shown in Figure 1a. Rb atoms are cooled and trapped in a 3D magneto-optical trap (MOT), from which they are loaded into a vertically oriented OL formed using a TEM$_{00}$-mode of a near-concentric in-vacuum optical cavity. The OL laser has a wavelength of $\lambda = 1064$ nm, for which $\alpha_{5D_{3/2}}$ is obtained. In the present work, the OL-induced light shifts are in the regime of several $h \times 1$ MHz, which places the experiment in a regime in which the $5D_{3/2}$ hyperfine structure tends to dominate the light shift (weak-field regime). This differs from [22], where the lattice was dominant and the $5D_{3/2}$ hyperfine structure was negligible (strong-field regime). While the lattice field is fairly weak in our present case, the field enhancement cavity is still essential in that it provides a clean TEM$_{00}$ OL field mode, in which the atoms are prepared. In Section 3, this will allow us to apply a well-defined model for the OL field generating the light shifts and the atom distribution in the OL. In addition to generating the $5D_{3/2}$ light-shifts to be measured, the lattice light also photo-ionizes the $5D_{3/2}$ atoms, which broadens the atomic levels and serves as a method for $|5D_{3/2}\rangle$-population readout via ion counting. Since the PI cross-section is known, the readout can be accurately modeled in the simulation in Section 3.
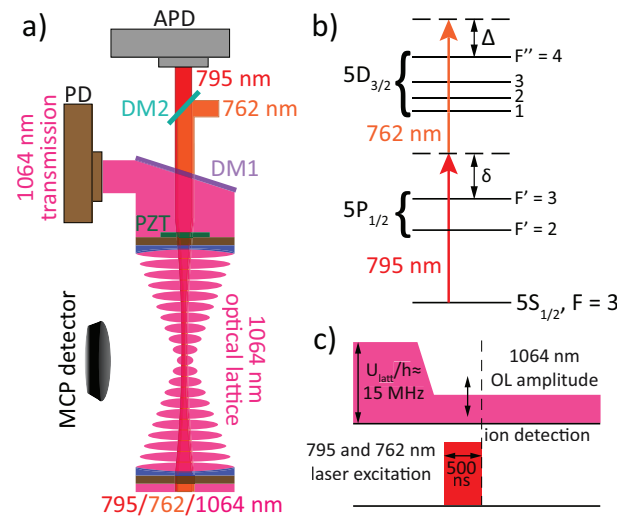

Figure 1. (Color online) Outline of experimental setup (**a**), utilized laser excitation scheme (not to scale) (**b**), and timing sequence of laser excitation and photoionization (**c**). "APD" avalanche photo-detector; "PD" photo-diode; "DM" dichroic mirror; "PZT" piezo-electric transducer. See text for details.

Two probe-laser beams at 795 nm and 762 nm (powers ~ 1 μW and ~ 50 μW before the cavity, respectively) are tuned by the means of two optical phase-locked loops (OPLLs) relative to fixed-frequency reference lasers that are locked to the relevant atomic transitions via saturated spectroscopy in Rb vapor cells. The probe lasers are coupled to the cavity to drive atoms from the $|5S_{1/2}, F = 3\rangle$ state to different HF states of the $5D_{3/2}$ level via the intermediate $|5P_{1/2}\rangle$ state, as shown in the level diagram in Figure 1b (magnetic quantum numbers suppressed in the kets). While coupling the probe-laser beams to the cavity is not required, doing so ensures mode-matching between the atom distribution in the OL and the probe-laser beam profiles. Throughout the data acquisition, the 795 nm laser is held at a fixed frequency with a detuning of $\delta = 0.9$ GHz with respect to field-free

$|5S_{1/2}, F = 3\rangle \rightarrow |5P_{1/2}, F' = 3\rangle$ transition. We scan the 762 nm laser frequency in 250-kHz steps to excite the Rb atoms into different HF states, $|5D_{3/2}, F''\rangle$. The detuning of the two-photon transition from the $|5S_{1/2}, F = 3\rangle \rightarrow |5D_{3/2}, F'' = 4\rangle$ transition is denoted Δ, as indicated in Figure 1b. We choose δ to be sufficiently large such that the observed spectra are the result of practically pure two-photon transitions without significant influence of the $5P_{1/2}$ state's HF structure (~ 361.6 MHz [50]). In addition, the detuning δ exceeds the OL light shifts by two orders of magnitude, which simplifies the analysis in Section 3. The large δ necessitates relatively large beam powers for the excitation beams, required to reach decent two-photon Rabi frequencies. (The probe-beam settings also contrast with those in [22], where small values of δ, low beams powers, and "step-wise" double-resonance spectroscopy were used.) Detailed schematics of cavity-mode stabilization and OPLLs are provided in [22].

After 10 ms of OL loading (full OL trap depth for atoms in the $5S_{1/2}$-level during the loading stage is $U_{latt} \approx h \times 15$ MHz), the OL power is ramped down by means of an acousto-optical modulator [not shown in Figure 1a] to a variable level, during which the $\sim$500 ns-long laser excitation is performed (see timing diagram in Figure 1c). The ions produced by PI due to 1064 nm light are guided through the electric-potential landscape applied via six electrodes (not shown in Figure 1a) that surround the optical cavity to a multichannel plate (MCP) detector. Ion spectra at each power level of 1064 nm light are recorded as a function of laser detuning for the subsequent analysis of the ac Stark shifts.

The ion signal observed at the lowest powers of 1064 nm light is, in part, attributed to Penning ionization, a process that has been found to be very effective in collisions of atoms in the $5D_{3/2}$ state [51,52]. Investigation of Penning and other ionization processes [53,54] using setups similar to ours is beyond the scope of the present work but could be a topic of future studies.

2.3. 1064 nm Power Calibration

As in similar measurements [38,55], it is important to properly calibrate the 1064 nm light intensity at the location of the atoms, I_{1064}. This is accomplished by measuring the transmitted 1064 nm power after the cavity output port with a photo-diode [PD in Figure 1a] that is connected to a transimpedance converter with a fixed gain (output voltage divided by photo-current). The transmitted power is proportional to the recorded voltage, denoted $P_{T,1064}$. Due to the linearity of the electronic circuit and the proportionality between I_{1064} and the power transmitted through the cavity, it is $I_{1064} = \gamma P_{T,1064}$.

To obtain the calibration factor γ, we measure spectra of the Rb $D1$ line in the absence of the 762 nm light for several OL intensities, for which the corresponding voltages $P_{T,1064}$ are recorded. To avoid saturation, we decrease the 795-nm power beam to $\sim$50 nW as measured in front of the cavity. An avalanche photodetector [APD in Figure 1a] installed after the cavity output port records the transmission of 795-nm light, T_{795} (see Figure 2 for an example). Appropriate dichroic mirrors (DM1 and DM2 in Figure 1a) eliminate the 762 nm and 1064 nm beams from the 795 nm transmission signal. Using known dynamic scalar polarizabilities of $5S_{1/2}$ [16,56,57] and $5P_{1/2}$ states [47] in ^{85}Rb at 1064 nm, the following expression for the ac Stark shift of the D1 line, $\Delta\nu_{D1}$, follows from Equation (1):

$$
\begin{aligned}
\Delta\nu_{D1} &= -(\alpha_{5P_{1/2}}^{(0)} - \alpha_{5S_{1/2}}^{(0)})\frac{I_{1064}}{2hc\epsilon_0} \\
&= -(\alpha_{5P_{1/2}}^{(0)} - \alpha_{5S_{1/2}}^{(0)})\frac{\gamma P_{T,1064}}{2hc\epsilon_0} \quad .
\end{aligned}
\tag{3}
$$

The AC shifts $\Delta\nu_{D1}$ are measured by comparing the $D1$-line spectra with the OL turned off and on. An example of this analysis is shown in Figure 2. The measurements of $\Delta\nu_{D1}$ and corresponding transmitted-power readings $P_{T,1064}$ then allow us to determine the calibration factor γ. Line centers are obtained from Gaussian fits. Since in the $D1$-line spectra with the OL turned on the line shapes are asymmetric (see Figure 2), for the fits with the OL turned on, we limit the fitting domains to regions localized around the transmission

minima, with fitting-domain widths that are small fractions of the spectroscopic line width. This procedure leads to relative uncertainties in $\Delta\nu_{D1}$ of $\gtrsim 10\%$. We reduce the final uncertainty in γ by analyzing spectra collected over a range of OL powers, $P_{T,1064}$. Moreover, as the $5P_{1/2}$ level has two HF states, we determine $\Delta\nu_{D1}$ for each of them. The final value of γ, shown in Table 1, is computed as a weighted average over transmitted powers $P_{T,1064}$ and over the $5P_{1/2}$ HFS states $F' = 2$ and $F' = 3$. The final relative uncertainty in γ is 8%.
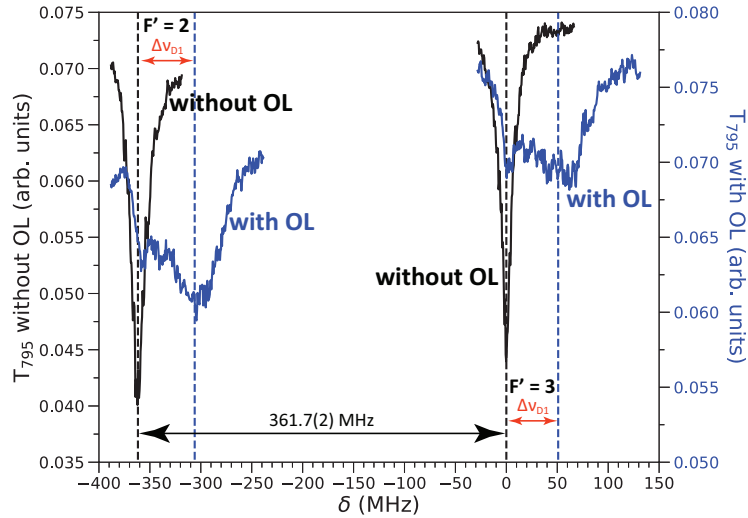

Figure 2. (Color online) Transmission of the 795 nm beam, T_{795}, as a function of detuning, δ, without (black solid line) and with (blue solid line) OL for calibration of I_{1064} using Equation (3). In all cases, the sample is prepared in identical ways with the lattice on during atom collection (depth $\sim h \times 15$ MHz; see Figure 1c). Both HF states of the $5P_{1/2}$ level ($F' = 2$ and 3) are resolved, as denoted in the Figure. Dashed vertical lines mark the 795-nm transmission minima without OL (black dashed lines at $\delta = 0$ and -362 MHz) and in the presence of the OL (blue dashed lines). The (not very pronounced) minima of the signals with OL that coincide with the black dashed lines at $\delta = 0$ and -362 MHz are due to atoms that are not in the OL; these atoms have no ac shifts. The broader signal minima, marked by the blue pair of dashed lines, correspond to atoms trapped near the intensity maxima of the OL; these atoms experience ac shifts due to the OL field. Analyzing the data in this figure, one finds $\Delta\nu_{D1} = 56(4)$ MHz, $P_{T,1064} = 152(9)$ mV for $F' = 2$ and $\Delta\nu_{D1} = 51(6)$ MHz, $P_{T,1064} = 160(6)$ mV for $F' = 3$.

Table 1. Summary of quantities used in the data analysis and the final results. Although polarizabilities are in SI units in most equations in the text, the polarizability values reported in this table are in atomic units for convenience.

Quantity	Value	Source
γ	37(3) GW/m^2/V	This experiment
$\alpha_{5S_{1/2}}^{(0)}$	687.3(5) a.u.	[57]
$\alpha_{5P_{1/2}}^{(0)}$	$-1226(18)$ a.u.	[47]
$\beta_{F''=3}$	5.59(39) MHz/GW/m^2	This experiment
$\beta_{F''=4}$	5.54(39) MHz/GW/m^2	This experiment
$\alpha_{5D_{3/2},F''=3}^{(0)}$	$-505(84)$ a.u.	Equation (5)
$\alpha_{5D_{3/2},F''=4}^{(0)}$	$-494(83)$ a.u.	Equation (5)
$\alpha_{5D_{3/2}}^{(0)}$	$-499(59)$ a.u.	Weighted average

The uncertainty in the recorded $P_{T,1064}$ values and the uncertainty of γ lead to final uncertainties of I_{1064}, using error propagation [58]. These are the main sources of uncertainty in the value of $\alpha_{5D_{3/2}}$ obtained in the next section. Improved cavity locking schemes

(with the current one being described in [22,49]), as well as a precise measurement of $\alpha_{5P_{1/2}}^{(0)}$, could lead to smaller uncertainties in future experiments.

2.4. Extracting $\alpha_{5D_{3/2}}$

We extract ac Stark shifts, $\Delta\nu_{F''}$, of different HF components of the $5D_{3/2}$ state by fitting Gaussian multi-peak profiles to the ion spectra. For the latter, we either acquire 5 to 10 scans and average them (at lowest 1064 nm power) or use single scans at good signal-to-noise ratios (at higher 1064 nm power, where PI is the most effective). Due to the HF structure of the Rb $5D_{3/2}$ state, the spectral lines from the two lowest HF states, $F'' = 1$ and $F'' = 2$ coalesce at lattice depths $U_{latt} \gtrsim h \times 1$ MHz (see Figure 3). Therefore, we restrict our data analysis to the $F'' = 3$ and $F'' = 4$ HF states, which are split by 18.6 MHz [23] and shift linearly with I_{1064}:

$$\Delta\nu_{F''} = \beta_{F''} I_{1064}, \tag{4}$$

with a fitting parameter $\beta_{F''}$ that is related to $\alpha_{5D_{3/2}}$ as shown below in Equation (5). Since the measurements are performed at low intensities of 1064 nm light and at large δ, the excitation of the atoms in the OL field is an off-resonant two-photon excitation in which the intermediate $5P_{1/2}$ states do not become populated. Hence, ac-Stark-shifts of the $5P_{1/2}$ states caused by the OL do not enter into Equation (4), and the polarizability of the $5P_{1/2}$-state is not explicitly required. (Note that the experimental intensity calibration factor $\gamma = I_{1064}/P_{T,1064}$, which is critical to extract the $5D_{3/2}$ polarizability, does require the polarizability of the $5P_{1/2}$-state.) With the experimental calibration factor $\gamma = I_{1064}/P_{T,1064}$, and utilizing the finding that the tensor polarizability $\alpha_{5D_{3/2}}^{(2)}$ is too small to produce measurable effects [22], Equations (1) and (4) yield

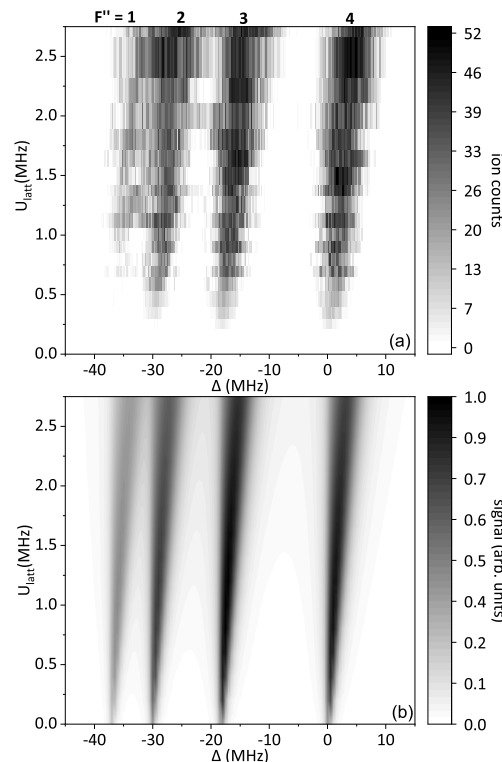$$\alpha_{5D_{3/2},F''}^{(0)} = \alpha_{5S_{1/2}}^{(0)} - 2hc\epsilon_0\beta_{F''} \quad . \tag{5}$$

Figure 3. Experimental ion spectra (**a**) and corresponding results of numerical simulations (**b**) as a function of two-photon detuning, Δ, and OL depth, U_{latt}. Parameters used for (**b**) are $\alpha_{5D_{3/2}}^{(0)} = -499$ a.u., $\alpha_{5D_{3/2}}^{(2)} = 0$ a.u., and $\sigma = 44$ Mb.

Since we analyze ac shifts of the two HF states $F'' = 3$ and 4, the final measurement result $\alpha_{5D_{3/2}}$ is reported in Table 1 as a weighted average over two values.

3. Results and Discussion

3.1. Determination of $\alpha_{5D_{3/2}}$

The obtained ion spectra at calibrated $U_{latt} = \frac{\alpha_{5S_{1/2}}}{2c\epsilon_0}\gamma P_{T,1064}$ are shown in Figure 3a. In a first cursory analysis, we compare the experimental spectra with a numerical simulation. The close resemblance of the experimental data with the results of the numerical simulations in Figure 3b is apparent. We attribute the larger broadening of the experimental spectra to the combined effects of the linewidths of the excitation lasers (both on the order of several 100 kHz), OL power fluctuations in the field enhancement cavity, and the MOT magnetic fields. The latter cannot be turned off during the measurement and may cause Zeeman broadening on the order of $\lesssim 1$ MHz. The Penning ionization process mentioned in Section 2.4, which is not included in our simulation, may enhance the experimental level broadening at low lattice depths U_{latt}. Moreover, the dominance of light-shift effects in the present system over Doppler effects has led us to adopt a "frozen" Boltzmann distribution of atoms in the simulation, which does not account for atomic-motion effects in the OL. Apart from the fact that the $F'' = 1$ HF component is somewhat weaker in the experiment than in the simulation, experimental and simulated data exhibit good qualitative agreement.

For a quantitative analysis, we extract $\nu_{F''}$ for the $F'' = 3$ and 4 HF components and follow the procedure described in Section 2.4. The results (dots) together with the fitting to Equation (4) (solid lines) are shown in Figure 4a,b for $F'' = 3$ and $F'' = 4$, respectively. The horizontal error bars are from the calibration of I_{1064}, as explained in Section 2.3, while the vertical error bars (which are smaller than the dots) reflect statistical uncertainties from the fits to the experimental spectra. It is apparent from Figure 4a,b that the error bars due to the I_{1064} calibration is the dominant source of uncertainty on $\beta_{F''}$ (see Table 1). We use only the two upper HF levels $F'' = 3$ and 4 for the data analysis because only these levels are well-discerned throughout the range of the applied I_{1064}-values. The lower levels $F'' = 1$ and 2 coalesce already at moderate I_{1064} due to their small HF splitting (see Figure 3), making the spectral fits unstable for those levels.
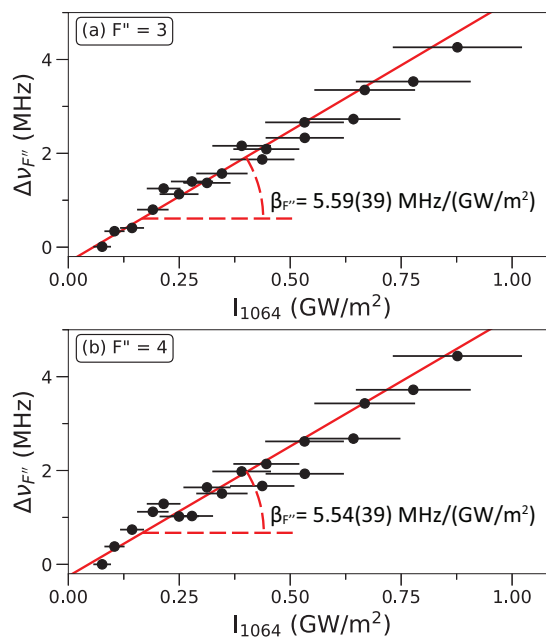

Figure 4. (Color online) ac Stark shifts, $\nu_{F''}$, vs. I_{1064} for $F'' = 3$ (**a**) and $F'' = 4$ (**b**). Dots with error bars are from experimental data. The solid lines are linear fits according to Equation (4).

The extracted values for $\alpha_{5D_{3/2}}$ of the $F'' = 3$ and four HF components as well as their weighted average are listed in Table 1. The final result, -499 ± 59 a.u., agrees within the uncertainty range with the previously reported value of -524 ± 17 [22]. The final uncertainty in the present paper is larger by a factor of ≈ 3.5 due to the sensitivity of the result to the calibration error in γ for the 1064 nm light intensity.

3.2. Discussion of the Result for $\alpha_{5D_{3/2}}$

The value of the present $\alpha_{5D_{3/2}}$-measurement relies on the fact that it is obtained in a different intensity regime than that used in [22] (low- vs. high-intensity limit). The present measurement is performed in the low-intensity regime, in which laser intensities are on the same order of magnitude as in contemporary cold-atom research [19,59–61]. The present measurement and the measurement in [22] exhibit different sets of systematic uncertainties. The observed agreement in $\alpha_{5D_{3/2}}^{(0)}$-values, within uncertainty limits, confirms the earlier result [22] and asserts that there are no critical omissions in the systematic effects affecting either of the measurements.

It is noteworthy that a previous theoretical analysis in [22] suggests that the dynamic *tensor* polarizability of the $5D_{3/2}$ state, and $\alpha_{5D_{3/2}}^{(2)}$ is very small. According to Equation (2), a substantial $\alpha_{5D_{3/2}}^{(2)}$ would cause a dependence of the ac shifts in Figures 3 and 4 and of the $\beta_{F''}$-values in Table 1 on the upper HF state F''. Furthermore, a substantial $\alpha_{5D_{3/2}}^{(2)}$ would cause line splittings of the F'' levels in Figures 3 and 4. The absence of such evidence in the measurements is consistent with $\alpha_{5D_{3/2}}^{(2)} \sim 0$. An actual measurement of $\alpha_{5D_{3/2}}^{(2)}$ is hampered, if not made impossible, by the line broadening in Figures 3 and 4, which is almost entirely due to PI of atoms by the 1064-nm OL light.

3.3. Quantum Interference at $\delta < 0$

The measurements reported above are performed at a large positive detuning, δ, from the $|5S_{1/2}, F = 3\rangle \rightarrow |5P_{1/2}, F' = 3\rangle$ transition to avoid any influence of the Rb $5P_{1/2}$-state HF structure on the result. In order to explore how the $5P_{1/2}$ HF structure affects the two-color $5D_{3/2}$ excitation spectra, we have performed additional simulations at $U_{latt} = h \times 2$ MHz with δ varied between -10 MHz and -350 MHz, scanning most of the range between $F' = 2$ and 3. The obtained simulated map is shown in Figure 5a as a function of δ and Δ as defined in Figure 1b. In this representation, the F'-resonances would appear as signal maxima lined up along horizontal lines at $\delta = -362$ MHz and 0 [just off-scale in Figure 5a], while the F''-resonances appear as vertical bars at Δ-values given by the respective F'' HF shifts. The signal in Figure 5a is characterized by some amount of line broadening along Δ due to lattice-induced PI, which sets a floor of several MHz for the linewidth in Δ. When approaching $\delta = -362$ MHz and 0 along the δ-axis, the signals become stronger and substantially broadened due to the near-resonant excitation of $5D_{3/2}$-atoms through the intermediate $F' = 2$ and 3 levels, respectively. In Figure 5a, we further observe signal dropouts on the $F'' = 2$ and $F'' = 3$-lines near $\delta \approx -75$ MHz and ≈ -200 MHz. The dropouts are due to quantum interference in the excitation amplitudes of the $F'' = 2$ and $F'' = 3$ HF states. Such an effect can be quite important in precision spectroscopy, with a recent precision measurement of the $2S \rightarrow 4P$ transition in atomic hydrogen for the determination of the Rydberg constant and the proton radius as a prominent example [62]. As δ is varied, the two-photon Rabi frequencies of the excitation channels $|5S_{1/2}, F = 3\rangle \rightarrow |5P_{1/2}, F' = 2\rangle \rightarrow |5D_{3/2}, F''\rangle$ and $|5S_{1/2}, F = 3\rangle \rightarrow |5P_{1/2}, F' = 3\rangle \rightarrow |5D_{3/2}, F''\rangle$ vary in relative strength due to their different, δ-dependent intermediate detunings. For $F'' = 2$ and 3, both two-photon Rabi frequencies are non-zero and have opposite signs in the displayed δ-range. Hence, at certain δ-values, destructive interference must occur, causing the signal dropouts in Figure 5a.
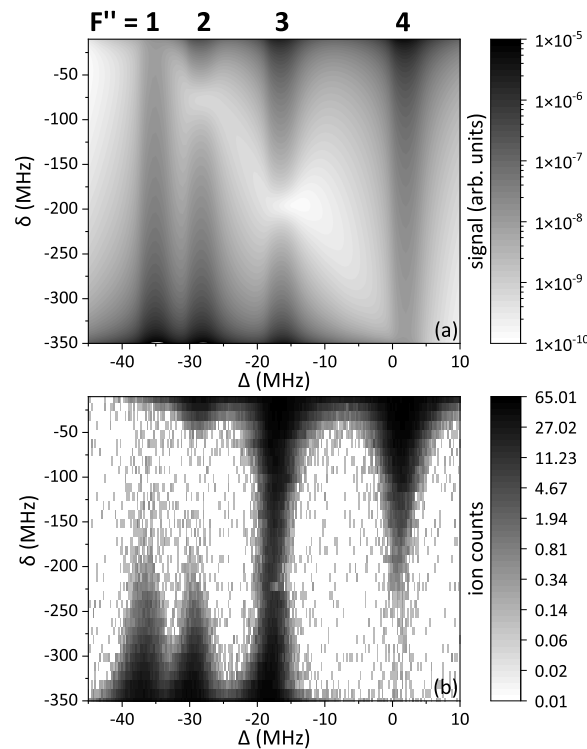
Figure 5. Simulated (**a**) and experimental (**b**) $5D_{3/2}$ ion spectra as a function of lower, δ, and upper, Δ, transition detunings at $U_{latt} \approx h \times 2$ MHz. See text for discussion.

In corresponding experimental data shown in Figure 5b, we generally observe the simulated behavior. Notable differences include the large strength of the $F'' = 3$-signal throughout the experimental data, as well as differences in the prominence of the signal dropouts caused by the destructive quantum interference. The discrepancies may be caused by optical-pumping and atomic-motion effects, which were both not included in the simulation. Furthermore, a "magic angle" technique [63,64] could be employed in future work to explore the dropouts and the mentioned discrepancy in more detail.

In advanced numerical work, which is beyond the scope of the present paper, one may have to consider the center-of-mass dynamics of the atoms on the lattice potentials, optical pumping, and coherent effects in the atom–field interaction. In the present experiment, the on-resonant Rabi frequencies on both transitions are on the order of 30 MHz, the atom–field interaction is 500 ns, the mechanical oscillation frequency of the $5S_{1/2}$-atoms in the wells is on the order of 0.2 MHz, and the distance the atoms travel transverse to the lattice axis due to their thermal energy is a fraction of a μm. For the far-off-resonant data in Figures 3 and 4, the far-off-resonant two-photon Rabi frequency is small ($\lesssim 1$ MHz), and the photon scattering rate (optical-pumping rate) is $\lesssim \times 10^6$ s^{-1}, justifying the simplified frozen-atom perturbative model we have adopted in Figure 3b. In advanced modeling that includes the aforementioned effects, we would expect only minor adjustments in the results.

For the closer-to-resonance work, the two-photon Rabi frequency is considerably larger, as it scales with the inverse of the intermediate detunings from the $5P_{1/2}$ hyperfine levels detuning δ, and a coherent sum over two channels must be taken as appropriate (see discussion several paragraphs above). In addition, close to the intermediate-state hyperfine resonances, double-resonant drive at the single-transition Rabi frequencies of several tens of MHz becomes dominant, causing the observed increase in linewidth near the intermediate-state hyperfine resonances. In that case, the optical-pumping rate approaches 10×10^6 s^{-1}. Coherent transients are also expected. Furthermore, close to the resonances, it will become important to consider the repulsive character of the excited-state light-shift potentials. Therefore, an improved model for the data in Figure 5 will have to include

optical pumping, coherent effects in the atom–field interaction, and the center-of-mass dynamics of the atoms on the lattice potentials. As the optical potentials are different for the various atomic states, in such future studies, one may have to implement certain techniques from computational molecular dynamics, such as the fewest-switches surface-hopping method [65,66].

4. Conclusions

In summary, we have reported a measurement of the dynamic polarizability of the Rb $5D_{3/2}$ state in 1064 nm optical fields in the "Zeeman" regime, where the ac shifts are less than the $5D_{3/2}$ hyperfine splittings. Our results show that the ac shifts of the $5D_{3/2}$ HF states approach the HF splittings already at moderate 1064-nm intensities, equivalent to commonly used optical-trap depths. Owing to the large $5D_{3/2}$ PI cross-section at 1064-nm wavelength, the spectroscopic lines exhibit significant broadening effects. In metrological applications [3,25,27,28] of cold $5D_{3/2}$ Rb atoms in 1064-nm laser traps, both ac shifts and PI broadening will have to be accounted for and minimized as needed. Future studies could be directed towards precise determination of the tensor contribution to the total polarizability, which was neglected in our analysis. To characterize the response of the $5D_{3/2}$ state to optical fields at a precision sufficient for this purpose, such studies could be performed at wavelengths longer than the PI threshold (1251.52 nm for Rb $5D_{3/2}$). Ac shifts and PI broadening should also be taken into account when using the Rb $5D_{3/2}$ state as an intermediate excitation level in experiments on Rydberg atoms and molecules [30–33]. Conversely, PI of Rb $5D_{3/2}$ atoms provides an efficient method to prepare cold ion clouds for research on non-neutral plasmas, allowing studies of highly-excited Rydberg atoms immersed in such plasmas [42,43,67–69].

Author Contributions: Conceptualization, A.D., R.C. and G.R.; methodology, A.D., R.C. and G.R.; software, A.D. and G.R.; validation, A.D., R.C. and G.R.; formal analysis, A.D.; investigation, A.D., R.C. and G.R.; resources, A.D., R.C. and G.R.; data curation, A.D.; writing—original draft preparation, A.D., R.C. and G.R.; writing—review and editing, A.D., R.C. and G.R.; visualization, A.D. and G.R.; supervision, G.R.; project administration, A.D., R.C. and G.R.; funding acquisition, G.R. All authors have read and agreed to the published version of the manuscript.

Data Availability Statement: The data that support the findings of this study are available upon reasonable request from the authors.

Conflicts of Interest: The authors declare no conflict of interest.

References

1. Ludlow, A.D.; Boyd, M.M.; Ye, J.; Peik, E.; Schmidt, P.O. Optical atomic clocks. *Rev. Mod. Phys.* **2015**, *87*, 637–701. [CrossRef]
2. Bloom, B.J.; Nicholson, T.L.; Williams, J.R.; Campbell, S.L.; Bishof, M.; Zhang, X.; Zhang, W.; Bromley, S.L.; Ye, J. An optical lattice clock with accuracy and stability at the 10^{-18} level. *Nature* **2014**, *506*, 71–75. [CrossRef] [PubMed]
3. Martin, K.W.; Phelps, G.; Lemke, N.D.; Bigelow, M.S.; Stuhl, B.; Wojcik, M.; Holt, M.; Coddington, I.; Bishop, M.W.; Burke, J.H. Compact Optical Atomic Clock Based on a Two-Photon Transition in Rubidium. *Phys. Rev. Appl.* **2018**, *9*, 014019. [CrossRef]
4. Saffman, M. Quantum computing with atomic qubits and Rydberg interactions: progress and challenges. *J. Phys. B* **2016**, *49*, 202001. [CrossRef]
5. Morgado, M.; Whitlock, S. Quantum simulation and computing with Rydberg-interacting qubits. *AVS Quantum Sci.* **2021**, *3*, 023501. [CrossRef]
6. Sedlacek, J.A.; Schwettmann, A.; Kübler, H.; Löw, R.; Pfau, T.; Shaffer, J.P. Microwave electrometry with Rydberg atoms in a vapour cell using bright atomic resonances. *Nat. Phys.* **2012**, *8*, 819–824. [CrossRef]
7. Holloway, C.L.; Gordon, J.A.; Jefferts, S.; Schwarzkopf, A.; Anderson, D.A.; Miller, S.A.; Thaicharoen, N.; Raithel, G. Broadband Rydberg Atom-Based Electric-Field Probe for SI-Traceable, Self-Calibrated Measurements. *IEEE Trans. Antennas Propag.* **2014**, *62*, 6169–6182. [CrossRef]

8. Anderson, D.A.; Sapiro, R.E.; Raithel, G. Rydberg Atoms for Radio-Frequency Communications and Sensing: Atomic Receivers for Pulsed RF Field and Phase Detection. *IEEE Aerosp. Electron. Syst. Mag.* **2020**, *35*, 48–56. [CrossRef]

9. Anderson, D.A.; Sapiro, R.E.; Raithel, G. A Self-Calibrated SI-Traceable Rydberg Atom-Based Radio Frequency Electric Field Probe and Measurement Instrument. *IEEE Trans. Antennas Propag.* **2021**, *69*, 5931–5941. [CrossRef]

10. Delone, N.B.; Krainov, V.P. AC Stark shift of atomic energy levels. *Physics-Uspekhi* **1999**, *42*, 669–687. [CrossRef]

11. Gerginov, V.; Beloy, K. Two-photon Optical Frequency Reference with Active ac Stark Shift Cancellation. *Phys. Rev. Appl.* **2018**, *10*, 014031. [CrossRef]

12. Martin, K.W.; Stuhl, B.; Eugenio, J.; Safronova, M.S.; Phelps, G.; Burke, J.H.; Lemke, N.D. Frequency shifts due to Stark effects on a rubidium two-photon transition. *Phys. Rev. A* **2019**, *100*, 023417. [CrossRef]

13. Safronova, M.S.; Arora, B.; Clark, C.W. Frequency-dependent polarizabilities of alkali-metal atoms from ultraviolet through infrared spectral regions. *Phys. Rev. A* **2006**, *73*, 022505. [CrossRef]

14. Topcu, T.; Derevianko, A. Dynamic polarizability of Rydberg atoms: Applicability of the near-free-electron approximation, gauge invariance, and the Dirac sea. *Phys. Rev. A* **2013**, *88*, 042510. [CrossRef]

15. Le Kien, F.; Schneeweiss, P.; Rauschenbeutel, A. Dynamical polarizability of atoms in arbitrary light fields: General theory and application to cesium. *Eur. Phys. J. D* **2013**, *67*, 92. [CrossRef]

16. Marinescu, M.; Sadeghpour, H.R.; Dalgarno, A. Dynamic dipole polarizabilities of rubidium. *Phys. Rev. A* **1994**, *49*, 5103–5104. [CrossRef]

17. Metcalf, H.; van der Straten, P. *Laser Cooling and Trapping*; Springer: New York, NY, USA, 1999; Volume 3.

18. Patsch, S.; Reich, D.M.; Raimond, J.M.; Brune, M.; Gleyzes, S.; Koch, C.P. Fast and accurate circularization of a Rydberg atom. *Phys. Rev. A* **2018**, *97*, 053418. [CrossRef]

19. Cardman, R.; Raithel, G. Circularizing Rydberg atoms with time-dependent optical traps. *Phys. Rev. A* **2020**, *101*, 013434. [CrossRef]

20. Grimm, R.; Weidemüller, M.; Ovchinnikov, Y.B. Optical Dipole Traps for Neutral Atoms. *Adv. At. Mol. Opt. Phys.* **2000**, *42*, 95–170. [CrossRef]

21. Weckesser, P.; Thielemann, F.; Hoenig, D.; Lambrecht, A.; Karpa, L.; Schaetz, T. Trapping, shaping, and isolating of an ion Coulomb crystal via state-selective optical potentials. *Phys. Rev. A* **2021**, *103*, 013112. [CrossRef]

22. Cardman, R.; Han, X.; MacLennan, J.L.; Duspayev, A.; Raithel, G. ac polarizability and photoionization-cross-section measurements in an optical lattice. *Phys. Rev. A* **2021**, *104*, 063304. [CrossRef]

23. Nez, F.; Biraben, F.; Felder, R.; Millerioux, Y. Optical frequency determination of the hyperfine components of the $5S_{1/2}$-$5D_{3/2}$ two-photon transitions in rubidium. *Opt. Commun.* **1993**, *102*, 432–438. [CrossRef]

24. Touahri, D.; Acef, O.; Clairon, A.; Zondy, J.J.; Felder, R.; Hilico, L.; de Beauvoir, B.; Biraben, F.; Nez, F. Frequency measurement of the $5S_{1/2}$(F = 3)-$5D_{5/2}$(F = 5) two-photon transition in rubidium. *Opt. Commun.* **1997**, *133*, 471–478. [CrossRef]

25. Hilico, L.; Felder, R.; Touahri, D.; Acef, O.; Clairon, A.; Biraben, F. Metrological features of the rubidium two-photon standards of the BNM-LPTF and Kastler Brossel Laboratories. *Eur. Phys. J. Appl. Phys.* **1998**, *4*, 219–225. [CrossRef]

26. Bernard, J.E.; Madej, A.A.; Siemsen, K.J.; Marmet, L.; Latrasse, C.; Touahri, D.; Poulin, M.; Allard, M.; Têtu, M. Absolute frequency measurement of a laser at 1556 nm locked to the $5S_{1/2}$-$5D_{5/2}$ two-photon transition in ^{87}Rb. *Opt. Commun.* **2000**, *173*, 357–364. [CrossRef]

27. Terra, O.; Hussein, H. An ultra-stable optical frequency standard for telecommunication purposes based upon the $5S_{1/2} \rightarrow 5D_{5/2}$ two-photon transition in rubidium. *Appl. Phys. B* **2016**, *122*, 27. [CrossRef]

28. Quinn, T.J. Practical realization of the definition of the metre, including recommended radiations of other optical frequency standards (2001). *Metrologia* **2003**, *40*, 103–133. [CrossRef]

29. Carr, C.; Tanasittikosol, M.; Sargsyan, A.; Sarkisyan, D.; Adams, C.S.; Weatherill, K.J. Three-photon electromagnetically induced transparency using Rydberg states. *Opt. Lett.* **2012**, *37*, 3858–3860. [CrossRef]

30. Thaicharoen, N.; Moore, K.; Anderson, D.; Powel, R.; Peterson, E.; Raithel, G. Electromagnetically induced transparency, absorption, and microwave-field sensing in a Rb vapor cell with a three-color all-infrared laser system. *Phys. Rev. A* **2019**, *100*, 063427. [CrossRef]

31. Duspayev, A.; Han, X.; Viray, M.A.; Ma, L.; Zhao, J.; Raithel, G. Long-range Rydberg-atom–ion molecules of Rb and Cs. *Phys. Rev. Res.* **2021**, *3*, 023114. [CrossRef]

32. Younge, K.C.; Anderson, S.E.; Raithel, G. Adiabatic potentials for Rydberg atoms in a ponderomotive optical lattice. *New J. Phys.* **2010**, *12*, 023031. [CrossRef]

33. Cardman, R.; MacLennan, J.L.; Anderson, S.E.; Chen, Y.J.; Raithel, G.A. Photoionization of Rydberg Atoms in Optical Lattices. *New J. Phys.* **2021**, *23*, 063074. [CrossRef]

34. Snigirev, S.; Golovizin, A.; Tregubov, D.; Pyatchenkov, S.; Sukachev, D.; Akimov, A.; Sorokin, V.; Kolachevsky, N. Measurement of the 5D-level polarizability in laser-cooled Rb atoms. *Phys. Rev. A* **2014**, *89*, 012510. [CrossRef]

35. Terra, O. Absolute frequency measurement of the hyperfine structure of the $5S_{1/2} - 5D_{3/2}$ two-photon transition in rubidium using femtosecond frequency comb. *Measurement* **2019**, *144*, 83–87. [CrossRef]

36. Sheng, D.; Pérez Galván, A.; Orozco, L.A. Lifetime measurements of the 5d states of rubidium. *Phys. Rev. A* **2008**, *78*, 062506. [CrossRef]

37. Aymar, M.; Robaux, O.; Wane, S. Central-field calculations of photoionisation cross sections of excited states of Rb and Sr^+ and analysis of photoionisation cross sections of excited alkali atoms using quantum defect theory. *J. Phys. B* **1984**, *17*, 993–1007. [CrossRef]

38. Duncan, B.C.; Sanchez-Villicana, V.; Gould, P.L.; Sadeghpour, H.R. Measurement of the Rb (5 $D_{5/2}$) photoionization cross section using trapped atoms. *Phys. Rev. A* **2001**, *63*, 043411. [CrossRef]

39. Pohl, T.; Pattard, T.; Rost, J.M. Coulomb Crystallization in Expanding Laser-Cooled Neutral Plasmas. *Phys. Rev. Lett.* **2004**, *92*, 155003. [CrossRef]

40. Viray, M.A.; Miller, S.A.; Raithel, G. Coulomb expansion of a cold non-neutral rubidium plasma. *Phys. Rev. A* **2020**, *102*, 033303. [CrossRef]

41. Schmid, S.; Härter, A.; Denschlag, J.H. Dynamics of a Cold Trapped Ion in a Bose-Einstein Condensate. *Phys. Rev. Lett.* **2010**, *105*, 133202. [CrossRef]

42. Secker, T.; Gerritsma, R.; Glaetzle, A.W.; Negretti, A. Controlled long-range interactions between Rydberg atoms and ions. *Phys. Rev. A* **2016**, *94*, 013420. [CrossRef]

43. Ewald, N.V.; Feldker, T.; Hirzler, H.; Fürst, H.A.; Gerritsma, R. Observation of Interactions between Trapped Ions and Ultracold Rydberg Atoms. *Phys. Rev. Lett.* **2019**, *122*, 253401. [CrossRef] [PubMed]

44. Dieterle, T.; Berngruber, M.; Hölzl, C.; Löw, R.; Jachymski, K.; Pfau, T.; Meinert, F. Transport of a Single Cold Ion Immersed in a Bose-Einstein Condensate. *Phys. Rev. Lett.* **2021**, *126*, 033401. [CrossRef]

45. Hu, Q.Q.; Freier, C.; Sun, Y.; Leykauf, B.; Schkolnik, V.; Yang, J.; Krutzik, M.; Peters, A. Observation of vector and tensor light shifts in ^{87}Rb using near-resonant, stimulated Raman spectroscopy. *Phys. Rev. A* **2018**, *97*, 013424. [CrossRef]

46. Chen, Y.J.; Gonçalves, L.F.; Raithel, G. Measurement of Rb $5P_{3/2}$ scalar and tensor polarizabilities in a 1064-nm light field. *Phys. Rev. A* **2015**, *92*, 060501(R). [CrossRef]

47. Neuzner, A.; Körber, M.; Dürr, S.; Rempe, G.; Ritter, S. Breakdown of atomic hyperfine coupling in a deep optical-dipole trap. *Phys. Rev. A* **2015**, *92*, 053842. [CrossRef]

48. MacLennan, J.L. Rydberg Molecules and Excitation of Lattice-Mixed Rydberg States in a Deep Ponderomotive Optical Lattice. Ph.D. Thesis, The University of Michigan, Ann Arbor, MI, USA, 2021.

49. Chen, Y.J.; Zigo, S.; Raithel, G. Atom trapping and spectroscopy in cavity-generated optical potentials. *Phys. Rev. A* **2014**, *89*, 063409. [CrossRef]

50. Steck, D.A. Rubidium 85 D Line Data, Revision 2021. Available online: http://steck.us/alkalidata (accessed on 8 August 2022).

51. Barbier, L.; Pesnelle, A.; Cheret, M. Theoretical interpretation of Penning and associative ionisation in collisions between two excited rubidium atoms. *J. Phys. B* **1987**, *20*, 1249–1260. [CrossRef]

52. Barbier, L.; Cheret, M. Experimental study of Penning and Hornbeck-Molnar ionisation of rubidium atoms excited in a high s or d level (5d ⩽ nl ⩽ 11s). *J. Phys. B* **1987**, *20*, 1229–1248. [CrossRef]

53. Cheret, M.; Barbier, L.; Lindinger, W.; Deloche, R. Penning and associative ionisation of highly excited rubidium atoms. *J. Phys. B* **1982**, *15*, 3463–3477. [CrossRef]

54. Barbier, L.; Djerad, M.T.; Chéret, M. Collisional ion-pair formation in an excited alkali-metal vapor. *Phys. Rev. A* **1986**, *34*, 2710–2718. [CrossRef] [PubMed]

55. Dinneen, T.P.; Wallace, C.D.; Tan, K.Y.N.; Gould, P.L. Use of trapped atoms to measure absolute photoionization cross sections. *Opt. Lett.* **1992**, *17*, 1706–1708. [CrossRef] [PubMed]

56. Bonin, K.D.; Kadar-Kallen, M.A. Theory of the light-force technique for measuring polarizabilities. *Phys. Rev. A* **1993**, *47*, 944–960. [CrossRef] [PubMed]

57. Arora, B.; Sahoo, B.K. State-insensitive trapping of Rb atoms: Linearly versus circularly polarized light. *Phys. Rev. A* **2012**, *86*, 033416. [CrossRef]

58. Taylor, J.R. *An Introduction to Error Analysis: The Study of Uncertainties in Physical Measurements*, 2nd ed.; University Science Books: Sausalito, CA, USA, 1996.

59. Anderson, S.E.; Younge, K.C.; Raithel, G. Trapping Rydberg Atoms in an Optical Lattice. *Phys. Rev. Lett.* **2011**, *107*, 263001. [CrossRef]

60. Gross, C.; Bloch, I. Quantum simulations with ultracold atoms in optical lattices. *Science* **2017**, *357*, 995–1001. [CrossRef]

61. Chomaz, L.; Ferrier-Barbut, I.; Ferlaino, F.; Laburthe-Tolra, B.; Lev, B.L.; Pfau, T. Dipolar physics: A review of experiments with magnetic quantum gases. *arXiv* **2022**, arXiv:2201.02672.

62. Beyer, A.; Maisenbacher, L.; Matveev, A.; Pohl, R.; Khabarova, K.; Grinin, A.; Lamour, T.; Yost, D.C.; Hänsch, T.W.; Kolachevsky, N.; et al. The Rydberg constant and proton size from atomic hydrogen. *Science* **2017**, *358*, 79–85. [CrossRef]

63. Sansonetti, C.J.; Simien, C.E.; Gillaspy, J.D.; Tan, J.N.; Brewer, S.M.; Brown, R.C.; Wu, S.; Porto, J.V. Absolute Transition Frequencies and Quantum Interference in a Frequency Comb Based Measurement of the ^{6,7}Li *D* Lines. *Phys. Rev. Lett.* **2011**, *107*, 023001. [CrossRef]

64. Brown, R.C.; Wu, S.; Porto, J.V.; Sansonetti, C.J.; Simien, C.E.; Brewer, S.M.; Tan, J.N.; Gillaspy, J.D. Quantum interference and light polarization effects in unresolvable atomic lines: Application to a precise measurement of the ^{6,7}Li D_2 lines. *Phys. Rev. A* **2013**, *87*, 032504. [CrossRef]

65. Tully, J.C. Molecular dynamics with electronic transitions. *J. Chem. Phys.* **1990**, *93*, 1061. [CrossRef]

66. Craig, C.F.; Duncan, W.R.; Prezhdo, O.V. Trajectory Surface Hopping in the Time-Dependent Kohn-Sham Approach for Electron-Nuclear Dynamics. *Phys. Rev. Lett.* **2005**, *95*, 163001. [CrossRef] [PubMed]
67. Weber, T.M.; Niederprüm, T.; Manthey, T.; Langer, P.; Guarrera, V.; Barontini, G.; Ott, H. Continuous coupling of ultracold atoms to an ionic plasma via Rydberg excitation. *Phys. Rev. A* **2012**, *86*, 020702. [CrossRef]
68. Anderson, D.A.; Raithel, G.; Simons, M.; Holloway, C.L. Quantum-optical spectroscopy for plasma electric field measurements and diagnostics. *arXiv* **2017**, arXiv:1712.08717.
69. Ma, L.; Paradis, E.; Raithel, G. DC electric fields in electrode-free glass vapor cell by photoillumination. *Opt. Express* **2020**, *28*, 3676–3685. [CrossRef] [PubMed]